

Jacob et al., 2013

1

1

2

Ordering state in orthopyroxene as determined by precession electron

3

diffraction.

4

5

REVISION III

6

7

Damien Jacob¹, Lukas Palatinus², Priscille Cuvillier¹, Hugues Leroux¹, Chiara Domeneghetti³

8

and Fernando Cámara⁴.

9

¹Unité Matériaux et Transformations, Université Lille1, CNRS UMR 8207, 59655 Villeneuve

10

d'Ascq, France

11

²Institute of Physics of the AS CR, 182 21 Prague, Czech Republic

12

³Dip.to di Scienze della Terra e dell'Ambiente, Università di Pavia, 27100-Pavia, Italy

13

⁴Dip.to di Scienze della Terra, Università di Torino, 10125-Torino, Italy.

14

15

* E-mail: damien.jacob@univ-lille1.fr

16

17

18
19

20 **Abstract**

21 Fe^{2+} and Mg distribution on octahedral M1 and M2 sites of the orthopyroxene
22 structure is an indicator of the cooling rate and closure temperature of the mineral. It is
23 generally obtained by single crystal X-ray diffraction, which is limited in spatial resolution. In
24 this work, we determine the cationic distribution at a sub-micron scale in a transmission
25 electron microscope using precession electron diffraction. Two orthopyroxene samples
26 coming from the same metamorphic rock are studied, a naturally ordered one and a disordered
27 one. The latter was obtained from the ordered sample by annealing at high temperature and
28 rapid quenching. Both samples have been first studied in X-ray diffraction and then in
29 precession electron diffraction. Intensities recorded in zone-axis precession electron
30 diffraction experiments have been quantitatively analyzed and compared to simulations,
31 taking into account dynamical interactions between diffracted beams. Our structure
32 refinement results are in good agreement with those obtained by single-crystal X-ray
33 diffraction. They enable to distinguish between the ordered sample and the disordered one in
34 terms of the observed molar fractions of Fe at M1 and M2 sites. We discuss the sensitivity of
35 the method as a function of experimental parameters. The larger dispersion of the results
36 obtained on the ordered specimen is attributed to structural heterogeneities inherent to the
37 sample.

38

39 **Keywords:** ordering, orthopyroxene, precession electron diffraction, site occupancy, structure
40 refinement, transmission electron microscopy.

41

Jacob et al., 2013

3

42

43

44

INTRODUCTION

45

46 Fe^{2+} and Mg distribution on octahedral M1 and M2 sites of the orthopyroxene (OPX)
47 structure is an indicator of the cooling rate and closure temperature of the mineral (Ganguly
48 1982; Ganguly et al. 1994; Stimpfl et al., 1999; Stimpfl et al., 2005). These data are of great
49 importance, as they permit the retrieval of the thermal history of the crystal (closure
50 temperature and cooling rate). The cationic distribution is generally accessible thanks to the
51 quantitative analysis of diffracted intensities as obtained by X-ray diffraction (XRD), leading
52 to the determination of atomic positions and site occupancies with a good accuracy.
53 Nevertheless, XRD is limited in spatial resolution. Contradictory results in cooling rate
54 determination based on site occupancies as determined by XRD have been explained by the
55 occurrence of microstructural features such as local variations of composition, exsolution
56 lamellae and Guinier-Preston zones (Zema et al, 1999; Cámara et al., 2000; Heinemann et al.,
57 2008). These features can only be revealed by transmission electron microscopy, whereas
58 XRD analysis generally leads to averaged information, which may induce misinterpretation.

59 In this work, we present results on site occupancy determination obtained at a
60 microscopic scale in a transmission electron microscope (TEM) using precession electron
61 diffraction (PED). Since its development in 1994 (Vincent and Midgley 1994), PED has
62 become an efficient and widely used method for solving structures of inorganic compounds
63 (Boulay et al. 2007 (perovskite related $\text{LaBaCuCoO}_{5.2}$ and $\text{Ba}_6\text{Mn}_5\text{O}_{16}$); Gemmi et al. 2007
64 (minerals uvarovite and åkermanite); Boullay et al. 2009 (mineral brownmillerite); Mugnaioli
65 et al. 2009 (inorganic salt BaSO_4); Gemmi et al. 2010 (titanate $\text{Li}_4\text{Ti}_8\text{Ni}_3\text{O}_{21}$); Hadermann et
66 al. 2010 (perovskite related $\text{Pb}_{13}\text{Mn}_9\text{O}_{25}$); White et al. 2010 (tin oxide Sn_3O_4); Hadermann et

Jacob et al., 2013

4

67 al. 2011 (mixed phosphate $\text{Li}_2\text{CoPO}_4\text{F}$); Klein et al. 2011 (oxides Mn_2O_3 and $\text{PbMnO}_{2.75}$;
68 Palatinus et al. 2011 (copper silicide-germanide $\text{Cu}_3(\text{Si}_3\text{Ge})$); Song et al. 2012
69 (hydroxyapatite)). At this stage, solving a structure means determining its unit cell
70 parameters, its space group and the position of most of the atoms within the unit cell.
71 Nevertheless, another important goal in structural analysis is the structure refinement, i.e. the
72 accurate determination of all the atomic positions and their occupancy. Unlike X-rays,
73 electrons interact strongly with matter and continuous exchange of electrons between
74 transmitted and diffracted beams occurs when they are passing through the crystal, leading to
75 so-called *dynamical effects*. Accurate simulation of electron diffraction data thus requires the
76 use of dynamical diffraction theory. In this context, the main advantage of PED for structure
77 solving is the reduction of the dynamical effects (Gjønnnes et al. 1998; Eggeman et al. 2010;
78 Sinkler and Marks, 2010), making the intensities more related to the square of the structure
79 factors of reflections. Nevertheless, to date very few attempts have been made to treat PED
80 data using dynamical theory for structural refinement (Own et al. 2006; Oleynikov et al. 2007;
81 Dudka et al. 2007; Sinkler et al. 2010). In most other cases the refinement was based on the
82 comparison of experimental diffracted intensities with simulated ones calculated in the
83 kinematical approximation, i.e. considering that diffracted intensities as proportional to the
84 square of the structure factors. The refinement results using kinematical approximation show
85 that dynamical effects must be taken into account, if accurate structure parameters are needed.
86 However, to our knowledge, only one structure refinement using dynamical theory has been
87 reported (Dudka et al. 2007) with silicon as a test sample. In this work, we show that when
88 the structure is partially known, dynamical analysis of intensities as obtained using PED leads
89 to reliable and reasonably accurate determination of structural parameters such as atomic
90 occupancy factors on specific sites of the structure. Applied to natural OPX samples, also
91 characterized by single crystal XRD, our PED analysis enables an unambiguous

92 discrimination between an ordered sample (natural, untreated) and a disordered one (heat-
93 treated and quenched).

94

95

EXPERIMENTAL

96

97 Specimen selection and heat treatments

98 The studied specimens are natural OPX ($\text{Mg}_{1.4}\text{Fe}_{0.6}\text{Si}_2\text{O}_6$) single crystals from
99 granulite rocks of the Wilson Terrane, North Victoria Land, Antarctica (crystal label B22,
100 Tribaudino and Talarico 1992). The ratio $\text{Mg}/(\text{Fe}+\text{Mg})$ is close to 0.70 as previously
101 determined by electron microprobe (Tarantino et al. 2002). Small amounts of Ca and other
102 minor elements such as Ti, Al, and Cr are also present. They were not considered in the
103 present analysis. Four crystals were selected and used for the X-ray single-crystal diffraction
104 to check for the homogeneity of the samples. To enable a direct comparison with disordered,
105 but otherwise similar sample, two of these crystals have also been heated for 48 hours at
106 1000°C. They were sealed (after alternately washing with nitrogen flux and vacuuming) into a
107 small silica tube together with an iron-wüstite buffer and then heated in a vertical furnace.
108 Inside the silica tube, the crystals and the buffer were put into two small separate Pt crucibles
109 to avoid contact between them. Heated samples were then quenched by dropping the tube into
110 cold water. One untreated and one heat-treated crystals were then selected for TEM analysis.

111

112 X-ray single-crystal diffraction and structure refinement

113 Intensity data were collected at the Dipartimento di Scienze della Terra e
114 dell'Ambiente, Università di Pavia, on a three-circle Bruker AXS SMART APEX
115 diffractometer, equipped with a CCD detector (graphite-monochromatized $\text{MoK}\alpha$ radiation, λ
116 = 0.71073 Å, 55 kV, 30 mA) and a monocap collimator. The Bruker SMART software

Jacob et al., 2013

6

117 package was used. A total of 3600 frames (frame resolution 512×512 pixels) were collected
118 with four different goniometer settings using the ω -scan mode (scan width: $0.2^\circ \omega$; exposure
119 time: 5-10 s/frame⁻¹; detector-sample distance: 4.02 cm). About 14500 reflections were
120 collected. Completeness of the measured data was achieved up to $37^\circ \theta$. The Bruker SAINT+
121 software was used for data reduction, including intensity integration, background and
122 Lorentz-polarization corrections. The semi-empirical absorption correction of Blessing
123 (1995), based on the determination of transmission factors for equivalent reflections, was
124 applied using the program SADABS (Sheldrick, 1996). The unit-cell parameters were
125 obtained by a least-squares procedure from the positions of about 8000 reflections in the θ -
126 range $3 - 37^\circ$. The observed F_o^2 values were then treated with a full-matrix least-squares
127 refinement in *Pbca* space group by SHELX-97 (Sheldrick, 2008), using individual weights
128 and the weighting scheme suggested by the program. No threshold or cutting of low intensity
129 reflections was applied, following the recommendations of Merli et al. (2002) suggested by
130 the leverage analysis applied to the orthopyroxene. The atomic scattering curves were taken
131 from International Tables for X-ray Crystallography (Ibers and Hamilton, 1974). Neutral vs.
132 ionized scattering factors were refined in all sites that are not involved in chemical
133 substitutions (Hawthorne et al. 1995) and complete ionization for Mg and Fe in M1 and M2
134 sites was assumed. The extinction correction was applied with the procedures of program
135 SHELX-97. In order to get a better comparability of the refinement results obtained using
136 XRD and PED data, structure refinements from XRD data have also been achieved in the
137 same conditions as previously described but limiting the resolution to that of PED data ($d =$
138 $0,7124 \text{ \AA}$).

139

140 **TEM observations and precession electron diffraction**

141 Thin foils for TEM observations were prepared from both the untreated and heat-
142 treated samples. Slabs about 50 nm thick normal to the [001] orientation have been cut from
143 the single crystal grains by focused ion beam (FIB) technique (FEI Strata DB 235 FIB-
144 FESEM) at IEMN (Institute of Micro and Nano Electronics, University Lille 1).

145 TEM observations were performed at University Lille 1 with a LaB₆ FEI Tecnai G2-
146 20 operated at 200 kV and equipped with a DIGISTAR precession system (Nanomegas). In
147 the PED technique, the incident beam is scanned at a constant precession semi-angle (ranging
148 typically from 1° to 4°) around the optical axis, in combination with an opposite and
149 synchronized descan of the transmitted and diffracted beams below the specimen (Vincent
150 and Midgley 1994). During the precession movement, the reciprocal lattice nodes are thus
151 swept through the Ewald sphere and integrated intensities over a large range of deviation
152 parameter S around the Bragg orientation are collected (compare Fig. 7). In PED, the incident
153 beam is never directed along the zone-axis so that dynamical interactions are reduced.
154 Microdiffraction (MD) and selected-area electron diffraction (SAED) patterns have been
155 acquired with optical axis aligned parallel to the [001] zone axis of the crystal. MD patterns
156 have been obtained using a nearly parallel probe of about 10-40 nm produced by a 10 μ m
157 condenser aperture. SAED patterns have been obtained using a defocused parallel beam and a
158 circular aperture selecting an illuminated area of about 250 nm in diameter. Precession angles
159 1.6° (heat-treated sample only), 2.4° and 2.8° have been used in order to test the sensitivity of
160 the method to the precession angle.

161

162

ANALYSIS OF PED DATA

163

164 **Dynamical calculations of intensities**

165 In a first approach, dynamical diffracted intensities have been calculated in the Bloch-
166 wave formalism using the JEMS software by P. Stadelmann (2004). Then, for systematic
167 comparison of simulated data with experimental ones and search for the best agreement, an
168 auxiliary program also using the Bloch-wave approach has been used. The full description of
169 the program and simulation conditions is presented in a dedicated paper (Palatinus et al.
170 2013). Basically, the simulation of diffracted intensities is obtained as an incoherent
171 summation of intensities sequentially calculated for a number N_{or} of orientations of the
172 incident beam along the precession circuit. N_{or} is an important parameter of the simulation:
173 the larger is N_{or} , the more accurate is the result. A few tests have been performed probing the
174 sensitivity of the simulated intensities on the choice of N_{or} . These tests showed that fixing N_{or}
175 to 150 is appropriate, as no improvement of the match could be obtained with larger N_{or} . For a
176 given structure file (see next paragraph), other main simulation parameters are the sample
177 thickness t , the orientation of the precession hollow cone axis with respect to the crystal
178 lattice and the number of diffracted beams to be taken into account for convergence of results.
179 In this preliminary work, no refinement of the beam orientation with respect to the crystal
180 orientation has been performed. We thus assumed that the crystal zone-axis used for the
181 diffraction pattern collection was perfectly parallel to the precession cone axis (normally
182 aligned along the optical axis of the microscope). This is generally not exactly fulfilled
183 experimentally, but we will see in the results section that this approximation leads to
184 reasonably accurate results provided the precession angle is sufficiently large. The number of
185 beams included in the calculation is described by two parameters, the maximum length of the
186 diffraction vectors g^{\max} (in \AA^{-1}) and the maximum excitation error S_g^{\max} . Following our
187 preliminary tests and results from Palatinus *et al.* (2013), the values of g^{\max} and S_g^{\max} have
188 been fixed to 2.0\AA^{-1} and 0.02\AA^{-1} , respectively, leading to a good compromise between
189 computation time and accuracy.

Jacob et al., 2013

9

190

191 **Comparison of simulated and experimental data**

192 For comparison with simulated data, integrated intensities were extracted from
193 experimental zone-axis patterns using the program PETS (Palatinus 2011, Palatinus et al.
194 2013). The output of the program consists of the list of reflections with their indices,
195 intensities and estimated standard deviations of the intensities $\sigma(I)$ calculated using the
196 standard background-signal-background method. Intensities were extracted up to $g^{\max} = 1.4$
197 \AA^{-1} . Typical values of the number of observed reflections ($I > 3\sigma$) are about 400, for about
198 500 total reflections. All the PED hkl files used in the present work are available as
199 supplementary material¹. The experimental data sets were then compared with several sets of
200 simulated intensities calculated from the OPX structure with variable Fe molar fraction
201 $X_{\text{Fe}}(\text{M1})$ and $X_{\text{Fe}}(\text{M2})$ on the M1 and M2 sites. Mg content is given by $X_{\text{Mg}}(\text{M1})=1-X_{\text{Fe}}(\text{M1})$
202 and $X_{\text{Mg}}(\text{M2})=1-X_{\text{Fe}}(\text{M2})$ as required by the pyroxene stoichiometry $(\text{Mg}_{2-x}\text{Fe}_x)\text{Si}_2\text{O}_6$, with x
203 $= X_{\text{Fe}}(\text{M1}) + X_{\text{Fe}}(\text{M2})$ the total Fe content (considering that minor elements are not taken into
204 account for this study; they account for < 0.04 apfu, i.e. $< 2\%$). All other structural
205 parameters are kept equal to the values deduced from XRD analysis (Table 1). No variation of
206 the cell parameters as a function of the order parameter has been considered since this effect
207 is negligible (Tarantino et al. 2002).

208 The present method is not a refinement method based on a least square procedure but
209 rather a grid search method. The best match between experimental and simulated intensities is
210 assessed by the lowest value of the weighted residual value $wR2$ given by:

211
$$wR2 = \sqrt{\frac{\sum w_g (I_g^o - I_g^c)^2}{\sum w_g (I_g^o)^2}}$$

¹ Deposit items are available via the MSA web site at <http://www.minsocam.org>.

Jacob et al., 2013

10

212 where I_g^o and I_g^c are the observed and calculated intensities, $w_g = \sigma^{-2} (I_g^o)$ and the summations
213 run over all reflections from the experimental data set.

214

215

RESULTS

216

217 XRD structure refinements

218

219 Table 1 reports the structure refinement results obtained with the high-resolution data
220 of both the untreated and heat-treated crystals. In Table 2 are summarized the atomic fractions
221 of Mg and Fe²⁺ at the M1 and M2 sites and the degree of order expressed as $Q = X_{\text{Fe}}(\text{M2}) -$
222 $X_{\text{Fe}}(\text{M1})$ of the untreated and heat-treated crystals, together with the refinement parameters
223 results. Results obtained limiting the resolution to that of PED data ($g^{\text{max}} = 1.4 \text{ \AA}^{-1}$) overlap
224 within their error bars with those obtained with the full set of XRD data. The four
225 crystallographic data of both crystals have been deposited¹

226 The untreated crystals are characterized by a high degree of Fe²⁺-Mg order on the
227 octahedral sites M1 and M2 of the OPX structure, with M2 sites mainly occupied by larger
228 Fe²⁺ cations. This ordered state is characteristic for slow cooling rate and low closure
229 temperature of the diffusion process (around 200°C) associated with the metamorphic origin
230 of the parent rocks (Tribaudino and Talarico 1992).

231 For the heat-treated samples, structure refinement results confirmed that the structure
232 was disordered, with a higher degree of mixing of the Fe²⁺ on both M1 and M2 sites.

233

234 TEM samples description

235 At the TEM scale, the untreated sample exhibits a homogenous microstructure made
236 of OPX containing a few planar defects and dislocations (Fig. 1a). The heat-treated sample
237 shows evidence of incongruent melting located at the very surface of the sample, leading to a

238 mixture of melt SiO₂ and Fe-rich olivine. The TEM study was performed in the lower part of
239 the sample, for which OPX is found to be homogeneous (Fig. 1b).

240

241 **Determination of cation occupancies by PED**

242 PED [001] zone-axis patterns have been acquired on both samples at several defect-
243 free areas separated by about 0.5 μm. Results are first presented for the heat-treated sample
244 and then for the untreated one.

245 *Heat-treated sample*

246 Selected area PED patterns have been acquired at three areas of the sample (located by
247 circles on Fig. 1b) and for precession angles of 1.6°, 2.4° and 2.8° (Fig. 2). As described in
248 the experimental section, the best match between experimental and simulated intensities is
249 searched by varying three parameters: the sample thickness t and the occupancies $X_{\text{Fe}}(\text{M1})$
250 and $X_{\text{Fe}}(\text{M2})$. Results giving the best agreement (lowest $wR2$ values) are summarized in Table
251 3 and plotted in Fig. 3. Uncertainty of the thickness is taken as a half of the thickness step
252 between individual simulations (4 nm). In the present work, uncertainties of the occupancies
253 are estimated as the variations of X_{Fe} leading to 0.1% variation on the minimum $wR2$ value.
254 This estimation may appear as somewhat artificial, but it is directly related to the curvature of
255 the $wR2$ surface as a function of $X_{\text{Fe}}(\text{M1})$ and $X_{\text{Fe}}(\text{M2})$ (Figs. 4a and b) and so to the actual
256 sensitivity of the method as a function of the experimental parameters (mainly the precession
257 angle). A more rigorous treatment based on a statistical analysis of the data as described in
258 Palatinus *et al.* (2013) leads to the same range of values for the uncertainties.

259 Results obtained with precession angle 1.6° are inconsistent with those obtained with
260 2.4 and 2.8°, leading to quite different $X_{\text{Fe}}(\text{M1})$ and $X_{\text{Fe}}(\text{M2})$ values (Fig. 3). A higher
261 dispersion of the results is also observed with precession angle 1.6° together with larger
262 estimated errors of the three parameters. The larger errors are associated with the shape of the

Jacob et al., 2013

12

263 $wR2$ surface at 1.6° precession angle, which is much flatter than those obtained at 2.4° and
264 2.8° (Fig. 4), making $wR2$ less sensitive to $X_{Fe}(M1)$ and $X_{Fe}(M2)$.

265 Results obtained with 2.4° and 2.8° data sets overlap within their standard deviation
266 for $X_{Fe}(M1)$ and $X_{Fe}(M2)$ whatever the observed area and the precession angle. The resulting
267 mean values and dispersions are $X_{Fe}(M1) = 0.144 \pm 0.008$ and $X_{Fe}(M2) = 0.447 \pm 0.010$.
268 These values are consistent with those derived from XRD data ($X_{Fe}(M1) = 0.155(2)$ and
269 $X_{Fe}(M2) = 0.438(2)$). The thicknesses as deduced from data sets with precession angles 2.4°
270 and 2.8° are also consistent, giving $t = 49 \pm 1.5$ nm for area 1, $t = 43 \pm 1.5$ for area 2 and $t =$
271 47.5 ± 1.5 nm for area 3.

272

273 *Untreated sample*

274 On the untreated sample, analysis has been performed using precession angles 2.4°
275 and 2.8° for three areas of the TEM specimen. Results are summarized in Table 4 and plotted
276 on Fig. 5. Note that for the first area, 5 data sets are available: 3 of them have been acquired
277 using microdiffraction (opt1Ap24, opt1Ap28 and opt1Bp28) and the remaining using
278 selected area diffraction. For areas 2 and 3, all the data have been acquired using selected area
279 diffraction.

280 Slight discrepancies are obtained at the three areas as a function of the precession
281 angles. Discrepancies are also observed between microdiffraction and selected area data sets
282 taken on area 1 with 2.4° precession angle (compare opt1Ap2.4 (microdiffraction) and
283 opt1Bp2.4 (selected area)). Results are more consistent using 2.8° precession angle (compare
284 opt1Ap2.8 and opt1Bp2.8 (microdiffraction) with opt1Cp2.8 (selected area)). Overall, a
285 larger dispersion of the results is observed compared to the heat-treated sample, leading to
286 mean values and dispersions $X_{Fe}(M1) = 0.069 \pm 0.016$ and $X_{Fe}(M2) = 0.551 \pm 0.028$. Despite

287 the small discrepancy between $X_{\text{Fe}}(\text{M1})$ obtained with PED and with XRD ($X_{\text{Fe}}(\text{M1}) =$
288 $0.029(2)$ and $X_{\text{Fe}}(\text{M2}) = 0.554(2)$), the agreement is once again satisfactory.

289

290

DISCUSSION

291

292 It follows clearly from Figs. 3 and 5 that the present method enables the distinction of
293 the OPX samples as a function of their ordering state. This distinction is emphasized in Fig. 6,
294 where all the data have been plotted together (only the inconsistent data with precession angle
295 1.6° have been removed). Furthermore, values obtained for site occupancies are globally
296 consistent with those obtained using XRD at the millimeter scale. To our knowledge, this is
297 the first successful demonstration that site occupancies can be determined quantitatively at
298 submicron scale using precession electron diffraction. Even if the dispersion of the results is
299 still high compared to that obtained using XRD and has to be lowered for quantitative
300 exploitation, this result opens the door to a wide range of applications in the field of the study
301 of minerals at the sub-micron scale and their potential use as geothermometers and
302 speedometers. In this section, we discuss the influence of experimental parameters on the
303 accuracy of the results, namely the precession angle and the initial orientation of the sample.
304 Possible structural heterogeneity in the natural sample is then inferred.

305

Influence of the precession angle and of the sample orientation

306 Two points require detailed discussion. First, concerning the heat-treated sample
307 (Table 3 and Fig. 3), results obtained with precession angle 1.6° are inconsistent with those
308 obtained with 2.4° and 2.8° and should be discarded. Second, results obtained on the various
309 areas of the natural sample with 2.4° and 2.8° precession angles do not strictly overlap within
310 their uncertainties (Table 4 and Fig. 5). These points suggest that the occupancy
311

312 determination could depend on the precession angle. However, calculation of diffracted
313 intensities for comparison with experimental data takes into account the value of the
314 precession angle and results should therefore not depend on it. Nevertheless, as described in
315 the section on data analysis, another important experimental parameter has not been taken into
316 account in the simulations of the PED intensities, namely the accurate orientation of the
317 sample with respect to the precession hollow cone axis. Let us call Θ the value of the angle
318 between the steady incident beam direction and the crystal zone axis (Fig. 7). When $\Theta = 0$
319 (Fig. 7a), the on-axis orientation is perfect and for each diffraction vector, the excitation error
320 S_g is equal to that of the opposite vector S_{-g} . When $\Theta \neq 0$ (Fig. 7b), $S_g \neq S_{-g}$ and consequently
321 $I_g \neq I_{-g}$. It is one of the principal advantages of the precession method to suppress the
322 influence of the sample misorientation by acquiring the integrated value of intensities I_g^{int}
323 (Fig. 7c) instead of a particular value $I_g(S_g)$ as in the steady beam configuration. To fully
324 exploit this advantage, the precession angle ϕ should be high with respect to Θ , otherwise
325 integration of the intensities is not complete and still depends on the orientation of the sample.
326 This is particularly true for the intense reflections close to the center of the diffraction pattern
327 (small g vectors). It is thus likely that the dispersion of the results as a function of the
328 precession angle occurs due to the imperfect alignment of the zone axis with respect to the
329 non-precessed electron beam, which is indeed not exactly known and difficult to quantify for
330 a given data set. This effect is most important for low precession angles, since the integration
331 of the intensities is then only partial. As a matter of fact, results obtained with the same data
332 sets but including beam orientation refinement (Palatinus *et al.* 2013) reveal a lower
333 sensitivity of the refined occupancies to the precession angle, and thus support the present
334 interpretation. Therefore, in a first approach, we suggest using high precession angles (larger
335 than 2°) for the data collection, and orienting the crystal very carefully. The residual effect of

336 misalignment should then be very small. Repeating the experiment several times on the same
337 area is a further means of improving the accuracy.

338

339 *Untreated sample heterogeneity*

340 For the untreated sample, there is a systematic discrepancy between the $X_{Fe}(M1)$ and
341 $X_{Fe}(M2)$ values deduced from PED and XRD. Furthermore, independently of the inaccuracy
342 of the sample orientation, results on $X_{Fe}(M1)$ and $X_{Fe}(M2)$ are more dispersed for the
343 untreated sample than for the heat-treated one (Fig. 6). All parameters for PED data
344 acquisition and analysis being equivalent for both samples (except for the actual beam
345 orientation, *cf* the previous section), this strongly suggests an influence of the samples
346 themselves. Indeed, the heat-treated (disordered) sample has been thermally homogenized at
347 high temperature, whereas no treatment has been made on the natural sample (ordered). The
348 untreated sample may thus present local composition or ordering heterogeneities. Such
349 structural heterogeneities may explain both the larger dispersion of the PED results and the
350 discrepancy between XRD and PED results obtained on this sample.

351 The heterogeneity of the untreated sample is highlighted when plotting the line of
352 constant composition in the graph of $X_{Fe}(M2)$ as a function of $X_{Fe}(M1)$ (Fig. 6). This line is
353 obtained using the relation $X_{Fe}(M2) = 2(1-y) - X_{Fe}(M1)$, where y is the ratio $Mg/(Fe+Mg)$.
354 Obviously, the dispersion of the results around the line drawn for $y = 0.70$ (as given by the
355 electron microprobe analysis at the grain scale) is much more pronounced for the untreated
356 sample than for the heat-treated one. At this point, two types of dispersion should be
357 distinguished: dispersion along the line corresponds to the variation of site occupancies (order
358 parameter) at constant composition, whereas results deviating from the line correspond to
359 compositional variations. In the case of the untreated sample, both kinds of dispersion are
360 present, suggesting order parameter variation as well as composition variation along the

Jacob et al., 2013

16

361 sample at a submicronic scale. The maximum Mg/(Mg+Fe) variation deduced from our
362 analysis is around 4% (see Table 5). While order parameter variation involving short-range
363 diffusion processes is plausible at this scale, composition variation is more unlikely. EDX
364 composition profile acquired across the studied areas revealed no composition fluctuation
365 higher than the sensitivity of the EDX method, i.e. around 2% on the Mg/(Fe+Mg) ratio. This
366 suggests that data sets resulting in a too high deviation (superior to 2%) from the constant
367 composition line are probably influenced by the imperfection of the model, especially by
368 neglecting the variation of the sample orientation. This is confirmed by results obtained using
369 orientation refinement (Palatinus et al. 2013), which are mainly dispersed along the constant
370 composition line, corresponding to ordering variations at a microscopic scale.

371

372

CONCLUSIONS

373

374 To our knowledge, this work on the structural ordering in orthopyroxene is the first
375 demonstration of a quantitative determination of site occupancies at submicron scale using
376 precession electron diffraction.. Even if quantitative exploitation of the results for deciphering
377 thermal history of the sample is still doubtful due to the high dispersion of the results,
378 precision is largely sufficient to distinguish between a natural metamorphic OPX ordered
379 structure from a disordered one obtained after annealing at high temperature and rapid
380 quenching. The method should be sensitive enough to characterize even possible intermediate
381 states of ordering.

382 There are other minerals in which the cationic distribution on non-equivalent sites
383 depends on the cooling rate and closure temperature. This is for instance the case of
384 clinopyroxene, for which equilibrium and kinetics of the disordering process has been already
385 well studied by single-crystal XRD for augitic compositions (Brizi et al. 2000; 2001) and for

Jacob et al., 2013

17

386 low-Ca pigeonitic compositions (Pasqual et al. 2000; Domeneghetti et al. 2005; Alvaro et al.
387 2011). Along with orthopyroxenes, the latter are thus considered as potential
388 geospeedometers. However, microtextural features present in many pyroxenes must be taken
389 into account when dealing with accurate determination of cation distributions by XRD. For
390 instance, orthopyroxenes and clinopyroxenes commonly show exsolution phenomena; in
391 some favorable cases these can be assessed properly and the presence of exsolution products
392 can be corrected for (Domeneghetti et al. 1996). Unfortunately, this has not been possible for
393 pigeonite crystals bearing augite exsolutions, which is by far the most common case for
394 pigeonite samples. This situation prevents the use of ordering processes in pigeonite as
395 geospeedometer for calculating cooling rates in meteorites. The use of PED thus opens an
396 immense field of application of geospeedometry using pigeonites, and may shed light on
397 many complicated cooling histories of terrestrial rocks or of planetary bodies.

398

399

400 **Acknowledgments**

401

402 The TEM national facility in Lille (France) is supported by the Conseil Regional du
403 Nord-Pas de Calais, the European Regional Development Fund (ERDF), and the Institut
404 National des Sciences de l'Univers (INSU, CNRS). D. Troadec (IEMN) is gratefully
405 acknowledged for the FIB samples preparation.

406 We are also very grateful to Dr. Stimpfl and a second anonymous reviewer for their
407 constructive comments leading to the improvement of the original manuscript.

408

Jacob et al., 2013

18

409

410

411 **References**

412

413 Alvaro, M., Cámara, F., Domeneghetti, M.C., Nestola, F., and Tazzoli, V. (2011) HT $P2_1/c$ -
414 $C2/c$ phase transition and kinetics of Fe^{2+} -Mg order-disorder of an Fe-poor pigeonite:
415 implications for the cooling history of ureilites. *Contributions to Mineralogy and Petrology*,
416 162(3), 599-613.

417

418 Boulahya, K., Ruiz-Gonzalez, L., Parras, M., Gonzalez-Calbet, J.M., Nickolsky, M.S., and
419 Nicolopoulos, S. (2007) Ab initio determination of heavy oxide perovskite related structures
420 from precession electron diffraction data. *Ultramicroscopy*, 107(6-7), 445-452.

421

422 Boullay, P., Dorcet, V., Perez, O., Grygiel, C., Prellier, W., Mercey, B., and Hervieu, M.
423 (2009) Structure determination of a brownmillerite $Ca_2Co_2O_5$ thin film by precession electron
424 diffraction. *Physical Review B*, 79(18), 8.

425

426 Blessing, R.H. (1995) An empirical correction for absorption anisotropy. *Acta*
427 *Crystallographica, A*, 51, 33-38.

428

429 Brizi, E., Molin, G.M., and Zanazzi, P.F. (2000) Experimental study of intracrystalline Fe^{2+} -
430 Mg exchange in three augite crystals: effect of composition on geothermometric calibration.
431 *American Mineralogist*, 85, 1375-1382.

432

433 Brizi, E., Molin, G.M., Zanazzi, P.F., and Merli, M. (2001) Ordering kinetics of Mg- Fe^{2+}
434 exchange in a $Wo_{43}En_{46}Fs_{11}$ augite. *American Mineralogist*, 86, 271-278.

Jacob et al., 2013

19

435

436 Cámara, F., Doukhan, J.-C., Domeneghetti, M.C., and Zema, M. (2000) A TEM study of Ca-
437 rich orthopyroxenes with exsolution products. *European Journal of Mineralogy*, 12(4), 735-
438 748.

439

440 Domeneghetti, M.C., Tazzoli, V., Boffa-Ballaran, T., and Molin, G.M. (1996) Orthopyroxene
441 from Serra de Magé meteorite: A structure refinement procedure for a *Pbca* phase coexisting
442 with *C2/c* exsolved phase. *American Mineralogist*, 81, 842-846.

443

444 Domeneghetti, M.C., Zema, M., and Tazzoli, V. (2005) Kinetics of Fe²⁺-Mg order-disorder in
445 *P2₁/c* pigeonite. *American Mineralogist*, 90, 1816-1823.

446

447 Dudka, A.P., Avilov, A.S., and Nicolopoulos, S. (2007) Crystal structure refinement using
448 Bloch-wave method for precession electron diffraction. *Ultramicroscopy*, 107(6-7), 474-482.

449

450 Eggeman, A.S., White, T.A., and Midgley, P.A. (2010) Is precession electron diffraction
451 kinematical? Part II: A practical method to determine the optimum precession angle.
452 *Ultramicroscopy*, 110(7), 771-777.

453

454 Ganguly, J. (1982) Mg-Fe order-disorder in ferromagnesian silicates. II. Thermodynamics,
455 kinetics and geological applications. In S.K. Saxena, Ed., *Advances in physical geochemistry*,
456 vol. 2, p. 58-99. Springer-Verlag, New York.

457

458 Ganguly, J. and Tazzoli, V. (1994) Fe²⁺-Mg Interdiffusion in ortho-pyroxene – retrieval from
459 the data on intracrystalline exchange-reaction. *American Mineralogist*, 79(9-10), 930-937.

Jacob et al., 2013

20

460

461 Gemmi, M. and Nicolopoulos, S. (2007) Structure solution with three-dimensional sets of
462 precessed electron diffraction intensities. *Ultramicroscopy*, 107(6-7), 483-494.

463

464 Gemmi, M., Klein, H., Rageau, A., Strobel, P., and Le Cras, F. (2010) Structure solution of
465 the new titanate $\text{Li}_4\text{Ti}_8\text{Ni}_3\text{O}_{21}$ using precession electron diffraction. *Acta Crystallographica*,
466 B66, 60-68.

467

468 Gjønnnes, K., Cheng, Y.F., Berg, B.S. Hansen, V.A.F., Gjønnnes, K., Cheng, Y.F., Berg, B.S.,
469 and Hansen, V. (1998) Corrections for multiple scattering in integrated electron diffraction
470 intensities. Application to determination of structure factors in the [001] projection of Al_mFe
471 *Acta Crystallographica*, A54, 102-119.

472

473 Hadermann, J., Abakumov, A.M., Tsirlin, A.A., Filonenko, V.P., Gonnissen, J., Tan, H.,
474 Verbeeck, J., Gemmi, M., Antipov, E.V., and Rosner, H. (2010) Direct space structure
475 solution from precession electron diffraction data: Resolving heavy and light scatterers in
476 $\text{Pb}_{13}\text{Mn}_9\text{O}_{25}$. *Ultramicroscopy*, 110(7), 881-890.

477

478 Hadermann, J., Abakumov, A.M., Turner, S., Hafideddine, Z., Khasanova, N.R., Antipov,
479 E.V., and Van Tendeloo, G. (2011) Solving the Structure of Li Ion Battery Materials with
480 Precession Electron Diffraction: Application to $\text{Li}_2\text{CoPO}_4\text{F}$. *Chemistry of Materials*, 23(15),
481 3540-3545.

482

Jacob et al., 2013

21

- 483 Hawthorne, F.C., Ungaretti, L., and Oberti, R. (1995) Site populations in minerals:
484 terminology and presentation of results of crystal-structure refinement. Canadian
485 Mineralogist, 33, 907–911.
486
- 487 Heinemann, R., Kroll, H., and Langenhorst, F. (2008) Relationship between Guinier-Preston
488 zones and the kinetics of the intracrystalline Fe²⁺, Mg exchange reaction in Johnstown
489 meteoritic orthopyroxene. European Journal of Mineralogy, 20, 551-561.
490
- 491 Ibers, J.A., and Hamilton, W.C., eds. (1974) International tables for X-ray crystallography
492 vol. 4, Birmingham, UK., Kynoch Press, 99–101.
493
- 494 Klein, H. (2011) Precession electron diffraction of Mn₂O₃ and PbMnO_{2.75}: solving structures
495 where X-rays fail. Acta Crystallographica, A67(3), 303-309.
496
- 497 Merli, M., Cámara, F., Domeneghetti, C., and Tazzoli, V. (2002) Leverage analysis of X-ray
498 single crystal diffraction data from orthopyroxene and pigeonite. European Journal of
499 Mineralogy, (14), 773–784.
500
- 501 Mugnaioli, E., Gorelik, T., and Kolb, U. (2009) "Ab initio" structure solution from electron
502 diffraction data obtained by a combination of automated diffraction tomography and
503 precession technique. Ultramicroscopy, 109(6), 758-765.
504
- 505 Oleynikov, P., Hovmoller, S., and Zou, X. D. (2007) Precession electron diffraction:
506 Observed and calculated intensities. Ultramicroscopy **107**, 523–533.
507

Jacob et al., 2013

22

- 508 Own, C. S., Marks, L. D., and Sinkler, W. (2006) Precession electron diffraction 1: multislice
509 simulation. *Acta Crystallographica section, A*62, 434–443.
510
- 511 Palatinus, L., Klementova, M., Drinek, V., Jarosova, M., and Petricek, V. (2011) An
512 Incommensurately Modulated Structure of η' -Phase of Cu_{3+x}Si Determined by Quantitative
513 Electron Diffraction Tomography. *Inorganic Chemistry* 50, 3743–3751.
514
- 515 Palatinus, L. (2011) PETS – program for analysis of electron diffraction data, Institute of
516 Physics of the AS CR, Prague, Czechia.
517
- 518 Palatinus, L., Jacob, D., Cuvillier, P., Klementova, M., Sinkler, W., and Marks, L.D. (2013)
519 Structure refinement from precession electron diffraction data. *Acta Crystallographica A*,
520 69(2), 171-188.
521
- 522 Pasqual, D., Molin, G., and Tribaudino, M. (2000) Single-crystal thermometric calibration of
523 Fe-Mg order-disorder in pigeonites. *American Mineralogist*, 85(7-8), 953-962.
524
- 525 Sheldrick, G.M. (1996) SADABS. Institut für Anorganische Chemie der Universität,
526 Göttingen, Germany.
527
- 528 Sheldrick, G.M., (2008) A short history of SHELX. *Acta Crystallographica A*, 64, 112–122.
529
- 530 Sinkler, W. and Marks, L.D. (2010) Characteristics of precession electron diffraction
531 intensities from dynamical simulations. *Zeitschrift für Kristallographie*, 225(2-3), 47-55.
532

Jacob et al., 2013

23

- 533 Song, K., Kim, Y.J., Kim, Y.I., and Kim, J.G. (2012) Application of theta-scan precession
534 electron diffraction to structure analysis of hydroxyapatite nanopowder. *Journal of Electron*
535 *Microscopy*, 61(1), 9-15.
- 536
- 537 Stadelmann, P. JEMS, Electron Microscopy Software, java version, CIME-EPFL, CH 1015
538 Lausanne, 2004.
- 539
- 540 Stimpfl, M., Ganguly, J., and Molin, G. (1999) Fe²⁺-Mg order-disorder in orthopyroxene:
541 equilibrium fractionation between the octahedral sites and thermodynamic analysis.
542 *Contributions to Mineralogy and Petrology*, 136(4), 297-309.
- 543
- 544 Stimpfl, M., Ganguly, J., and Molin, G. (2005) Kinetics of Fe²⁺-Mg order-disorder in
545 orthopyroxene: experimental studies and applications to cooling rates of rocks. *Contributions*
546 *to Mineralogy and Petrology*, 150(3), 319-334.
- 547
- 548 Tarantino, S.C., Domeneghetti, M.C., Carpenter, M.A., Shaw, C.J.S., and Tazzoli, V. (2002)
549 Mixing properties of the enstatite-ferrosilite solid solution: I. A macroscopic perspective.
550 *European Journal of Mineralogy*, 14(3), 525-536.
- 551
- 552 Tribaudino, M. and Talarico, F. (1992) Orthopyroxenes from granulite rocks of the Wilson
553 Terrane (Victoria Land, Antarctica); crystal chemistry and cooling history. *European Journal*
554 *of Mineralogy*, 4(3), 453-463.
- 555
- 556 Vincent, R. and Midgley, P.A. (1994) Double conical beam-rocking system for measurement
557 of integrated electron diffraction intensities. *Ultramicroscopy*, 53(3), 271-282.

Jacob et al., 2013

24

558

559 White, T.A., Moreno, M.S., and Midgley, P.A. (2010) Structure determination of the
560 intermediate tin oxide Sn_3O_4 by precession electron diffraction. *Zeitschrift Fur*
561 *Kristallographie*, 225(2-3), 56-66.

562

563 Zema, M., Domeneghetti, M.C., and Tazzoli, V. (1999) Order-disorder kinetics in
564 orthopyroxene with exsolution products. *American Mineralogist*, 84(11-12), 1895-1901.

565

Jacob et al., 2013

25

566

567

568 **Table and Figure captions**

569

570 **Table 1:** Structure refinement results obtained with the XRD high-resolution data from both
571 the untreated and heat-treated crystals.

572

573 **Table 2:** Refined molar fractions of Fe and Mg on M1 and M2 sites of the orthopyroxene
574 structure as deduced from XRD.

575

576 **Table 3:** Refinement results for PED data sets obtained on the heat-treated sample. Labels
577 include the area location (1, 2 or 3) and the precession angle. All data sets were collected
578 using selected area diffraction.

579

580 **Table 4:** Refinement results for PED data sets obtained on the untreated sample. Labels
581 include the area location (1, 2 or 3) and the precession angle. All data sets were collected
582 using selected area electron diffraction except oplt1Ap2.4, oplt1Ap2.8 and oplt1Bp2.8, which
583 correspond to microdiffraction.

584

585
586

587 **Figure 1:** TEM images of (a) the natural sample and (b) the annealed sample. Circles indicate
588 the analyzed areas (1, 2 and 3).

589

590 **Figure 2:** [001] zone-axis PED pattern (precession angle 2.8°) obtained on the heat-treated
591 sample. The dashed circle corresponds to the resolution limit $g^{\max} = 1.4 \text{ \AA}^{-1}$ for data
592 extraction.

593

594 **Figure 3:** Plot of $X_{\text{Fe}}(\text{M2})$ versus $X_{\text{Fe}}(\text{M1})$ for the heat-treated sample. Squares: precession
595 angle 1.6° , triangles: 2.4° and circles: 2.8° . Colors correspond to studied areas on the TEM
596 sample (see Fig. 1) (red: area 1, green: area 2, blue: area 3). The black star corresponds to
597 XRD data as obtained on the single crystal (error bars ca. size of the symbol).

598

599 **Figure 4:** Plot of $wR2$ as a function of $X_{\text{Fe}}(\text{M1})$ and $X_{\text{Fe}}(\text{M2})$ for the heat-treated sample. a)
600 Precession angle 2.8° , area 3. b) Precession angle 1.6° , area 2.

601

602 **Figure 5:** Plot of $X_{\text{Fe}}(\text{M2})$ versus $X_{\text{Fe}}(\text{M1})$ for the untreated sample. Triangles: precession
603 angle 2.4° and circles: precession angle 2.8° . Colors correspond to studied areas on the TEM
604 sample (see Fig. 1) (red: area 1, green: area 2, blue: area 3). The black star corresponds to
605 XRD data as obtained as obtained on the single crystal (error bars ca. size of the symbol).

606

607 **Figure 6:** Plot of $X_{\text{Fe}}(\text{M2})$ versus $X_{\text{Fe}}(\text{M1})$ for the untreated (blue) and heat-treated (red)
608 samples. Black stars correspond to XRD data (error bars ca. size of the symbol). The dashed-
609 line corresponds to the constant composition line with $\text{Mg}/(\text{Mg}+\text{Fe}) = 0.70$.

610

Jacob et al., 2013

27

611 **Figure 7:** Sketch of the variation of the intensity of a g diffraction vector as a function of the
612 orientation of the incident beam. S_g is the vector pointing from the reciprocal lattice node to
613 the Ewald sphere. S_g is positive when oriented along the beam direction and negative
614 elsewhere. (a) The incident beam is perfectly aligned along the zone axis and $S_g = S_{-g}$. (b) The
615 incident beam is tilted with an angle ϕ from the zone-axis orientation. Then $S_g \neq S_{-g}$. (c)
616 When the beam is rotated, the intensities are integrated along the S values. For the integration
617 to be sufficiently complete, the precession angle has to be high enough.
618

619
620
621
622
623
624
625

Table 1

Untreated crystal (high resolution data)

<i>a</i> (Å)	<i>b</i> (Å)	<i>c</i> (Å)	Unit-cell volume (Å ³)	Space group		
18.2810(7)	8.8732(4)	5.2070(2)	844.63(6)	<i>Pbca</i>		
<i>Structure parameters:</i>						
Site	<i>x/a</i>	<i>y/b</i>	<i>z/c</i>	Occupancy	<i>U</i> (Å ²)	Site multiplicity
SiA	0.271544(14)	0.34092(3)	0.05148(5)	1	0.00664(6)	8c
SiB	0.473884(14)	0.33679(3)	0.79705(5)	1	0.00664(6)	8c
O1A	0.18346(4)	0.33838(8)	0.04147(14)	1	0.00799(12)	8c
O1B	0.56251(4)	0.33764(8)	0.79832(14)	1	0.00814(12)	8c
O2A	0.31114(4)	0.50118(8)	0.05038(15)	1	0.00948(12)	8c
O2B	0.43369(4)	0.48497(8)	0.69471(14)	1	0.00976(12)	8c
O3A	0.30269(4)	0.22822(9)	-0.17338(14)	1	0.01049(13)	8c
O3B	0.44727(4)	0.19933(9)	0.59741(15)	1	0.01011(12)	8c
M1 (Fe ²⁺)	0.375580(18)	0.65446(4)	0.87128(7)	0.029(2)	0.00754(11)	8c
M1 (Mg ²⁺)	0.375580(18)	0.65446(4)	0.87128(7)	0.971(2)	0.00754(11)	8c
M2 (Fe ²⁺)	0.378034(11)	0.48345(2)	0.36509(4)	0.554(2)	0.00981(7)	8c
M2 (Mg ²⁺)	0.378034(11)	0.48345(2)	0.36509(4)	0.446(2)	0.00981(7)	8c

626
627
628
629
630
631

Heat-treated crystal (high resolution data)

<i>a</i> (Å)	<i>b</i> (Å)	<i>c</i> (Å)	Unit-cell volume (Å ³)	Space group		
18.3022(14)	8.8816(7)	5.2082(4)	846.6(1)	<i>Pbca</i>		
<i>Structure parameters:</i>						
Site	<i>x/a</i>	<i>y/b</i>	<i>z/c</i>	Occupancy	<i>U</i> (Å ²)	Site multiplicity
SiA	0.271647(15)	0.34083(3)	0.05069(5)	1	0.00705(7)	8c
SiB	0.473781(15)	0.33678(3)	0.79655(6)	1	0.00699(7)	8c
O1A	0.18360(4)	0.33901(8)	0.03946(15)	1	0.00863(13)	8c
O1B	0.56236(4)	0.33842(8)	0.79762(14)	1	0.00870(13)	8c
O2A	0.31119(4)	0.50097(8)	0.04912(15)	1	0.01006(13)	8c
O2B	0.43343(4)	0.48423(8)	0.69310(15)	1	0.01035(13)	8c
O3A	0.30274(4)	0.22748(9)	-0.17301(14)	1	0.01083(13)	8c
O3B	0.44741(4)	0.19873(9)	0.59763(14)	1	0.01065(13)	8c
M1 (Fe ²⁺)	0.375724(15)	0.65432(3)	0.87012(6)	0.155(2)	0.00805(10)	8c
M1 (Mg ²⁺)	0.375724(15)	0.65432(3)	0.87012(6)	0.845(2)	0.00805(10)	8c
M2 (Fe ²⁺)	0.377827(12)	0.48401(3)	0.36401(4)	0.438(2)	0.01025(8)	8c
M2 (Mg ²⁺)	0.377827(12)	0.48401(3)	0.36401(4)	0.562(2)	0.01025(8)	8c

632
633

634

635 **Table 2**

636

	Untreated crystal		Heat treated crystal	
	Full data Set	Low Res. 0.714 Å	Full data set	Low Res. 0.714 Å
X _{Fe} (M1)	0.029(2)	0.028(3)	0.155(2)	0.154(3)
X _{Mn} (M1)	0.971(2)	0.972(3)	0.845(2)	0.846(3)
X _{Fe} (M2)	0.554(2)	0.555(3)	0.438(2)	0.439(3)
X _{Mn} (M2)	0.446(2)	0.445(3)	0.562(2)	0.561(3)
Mg/(Fe+Mg)	0.709(3)	0.709(3)	0.704(3)	0.704(3)
$Q = X_{Fe}(M2) - X_{Fe}(M1)$	0.525(3)	0.527(3)	0.283(3)	0.285(3)
R ₁ (%)	2.73	2.41	3.07	2.66
wR2	6.64	5.99	7.41	6.81
n. of I/σ > 4	2090	1187	2039	1172
n. refl. tot.	2209	1209	2219	1215
ref. param.	93	93	93	93
Goof	1.199	1.172	1.144	1.178

637

638

639

640

641 **Table 3**

642

643

dataset	wR2	t (nm)	X _{Fe} (M1)	X _{Fe} (M2)	Q*	Mg/(Fe+Mg)
precession angle: 1.6°						
opht1p1.6	12.88	52(2)	0.200(15)	0.420(15)	0.220(15)	0.69
opht2p1.6	13.18	46(2)	0.235(15)	0.415(15)	0.180(15)	0.68
opht3p1.6	20.58	49(2)	0.280(15)	0.420(15)	0.140(15)	0.65
precession angle: 2.4°						
opht1p2.4	6.77	49(2)	0.147(10)	0.430(10)	0.283(15)	0.71
opht2p2.4	9.53	43(2)	0.134(10)	0.441(10)	0.307(15)	0.71
opht3p2.4	12.30	49(2)	0.140(10)	0.452(10)	0.312(15)	0.70
precession angle: 2.8°						
opht1p2.8	7.38	49(2)	0.154(10)	0.442(10)	0.288(20)	0.70
opht2p2.8	8.66	43(2)	0.134(10)	0.458(10)	0.324(20)	0.70
opht3p2.8	11.04	46(2)	0.154(10)	0.458(10)	0.304(20)	0.69

644

645 *Q = X_{Fe}(M2) - X_{Fe}(M1)

646

647

Jacob et al., 2013

31

648

649

650 **Table 4**

651

652

dataset	$wR2$	t (nm)	$X_{Fe}(M1)$	$X_{Fe}(M2)$	Q^*	Mg/(Fe+Mg)
precession angle: 2.4°						
oplt1Ap2.4 ¹	12.80	43(2)	0.030(10)	0.582(10)	0.552(15)	0.69
oplt1Bp2.4	9.42	40(2)	0.067(10)	0.544(10)	0.447(15)	0.69
oplt2p2.4	7.39	40(2)	0.092(10)	0.502(10)	0.410(15)	0.70
oplt3p2.4	17.89	40(2)	0.081(10)	0.572(10)	0.491(15)	0.67
precession angle: 2.8°						
oplt1Ap2.8 ¹	9.60	43(2)	0.072(10)	0.544(10)	0.472(15)	0.69
oplt1Bp2.8 ¹	9.35	40(2)	0.072(10)	0.535(10)	0.463(15)	0.70
oplt1Cp2.8	9.26	40(2)	0.067(10)	0.563(10)	0.496(15)	0.69
oplt2p2.8	15.11	40(2)	0.072(10)	0.595(10)	0.523(15)	0.67
oplt3p2.8	10.90	40(2)	0.072(10)	0.526(10)	0.454(15)	0.70

653

654 $*Q = X_{Fe}(M2) - X_{Fe}(M1)$

655 ¹microdiffraction

656

657

658

659

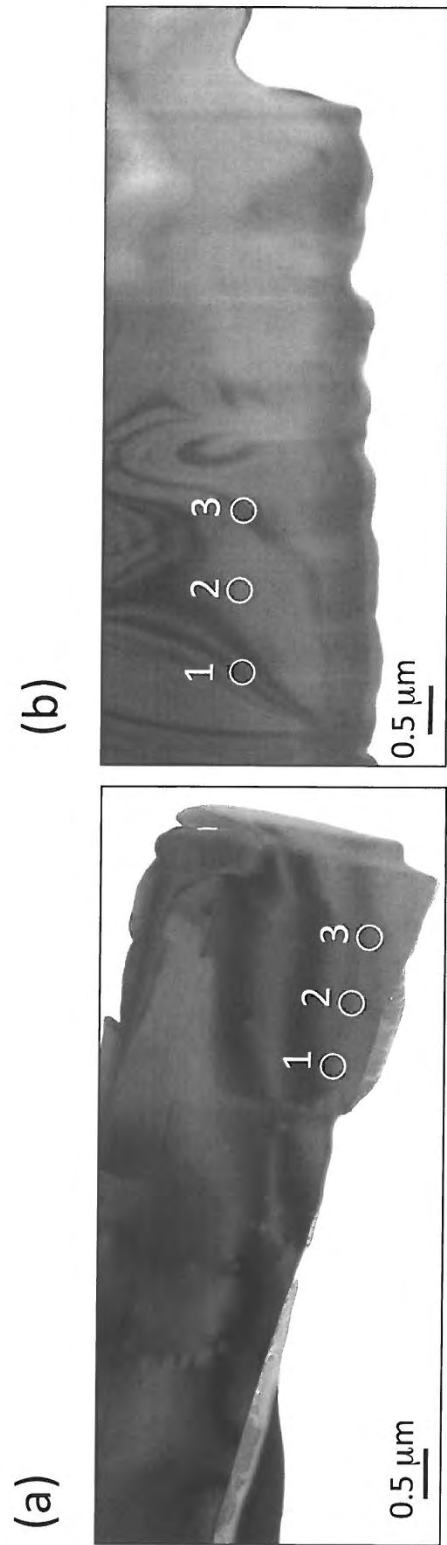


Figure 1

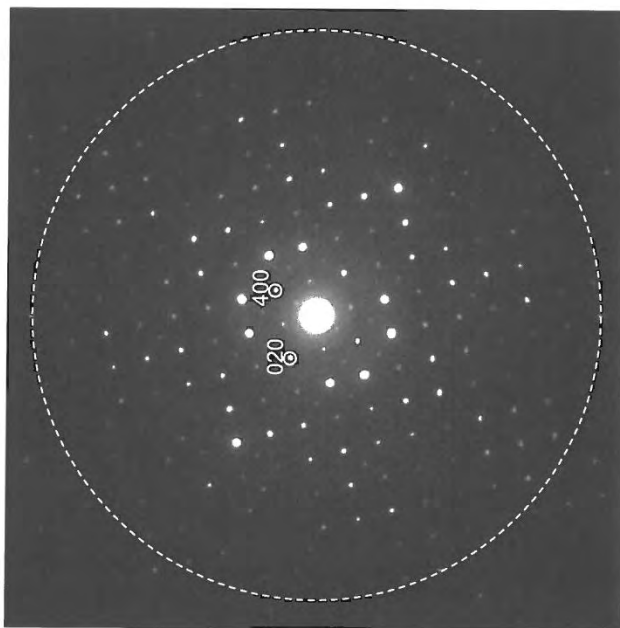


Figure 2

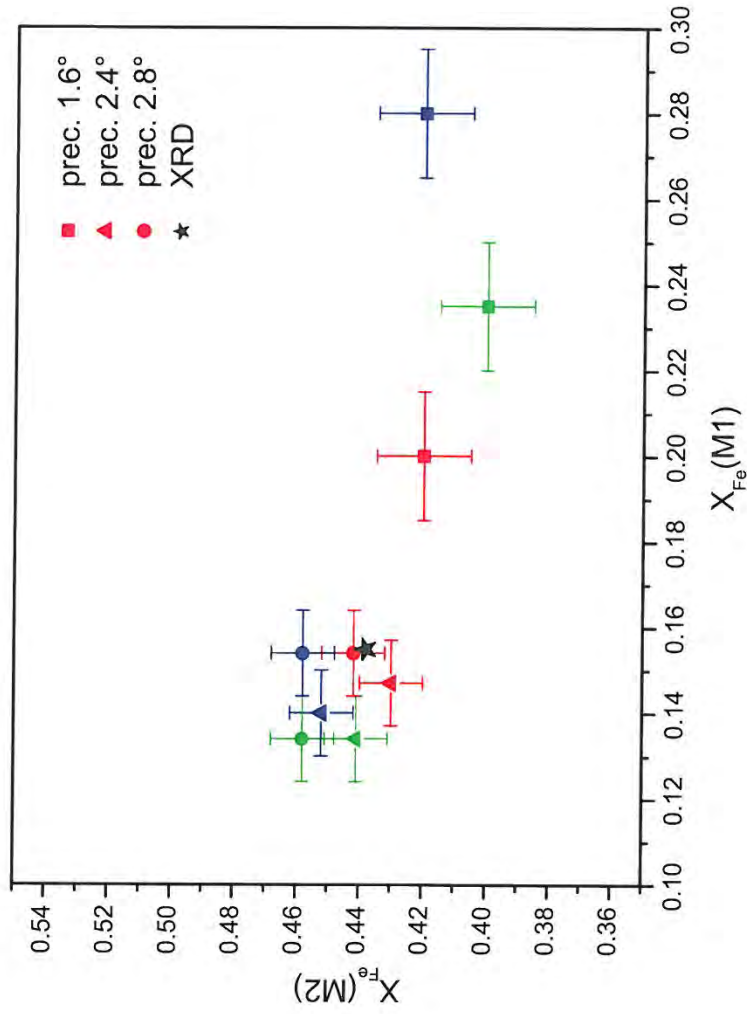


Figure 3

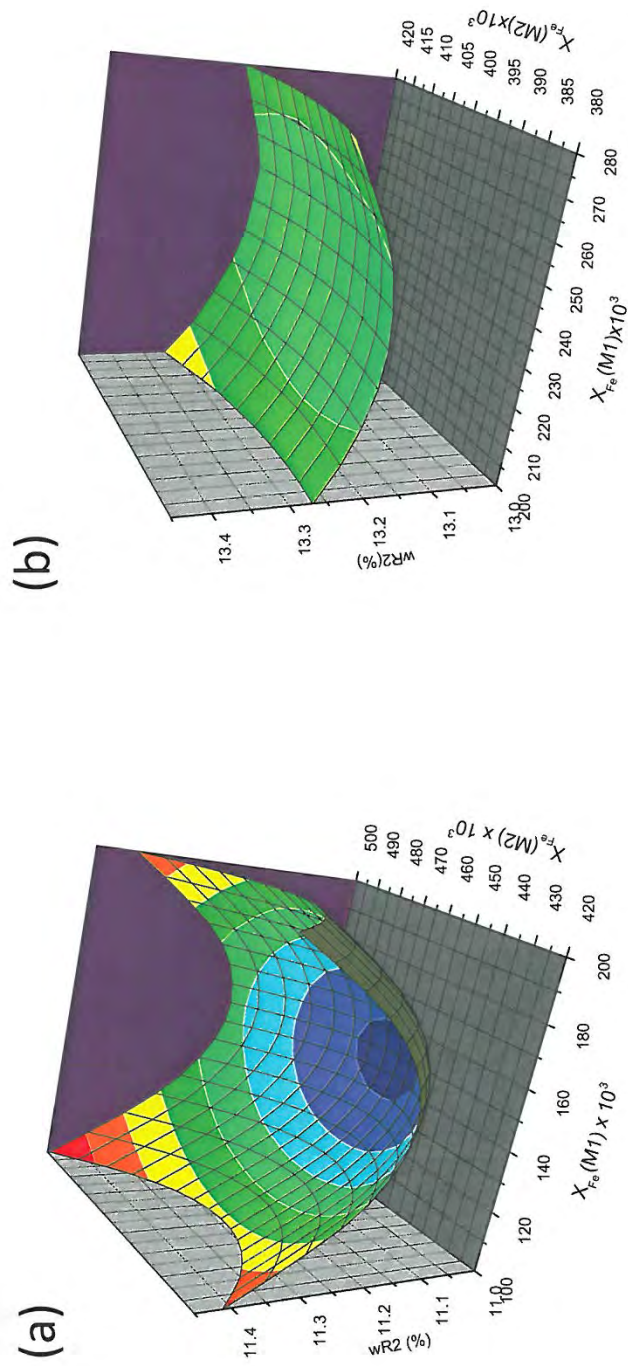


Figure 4

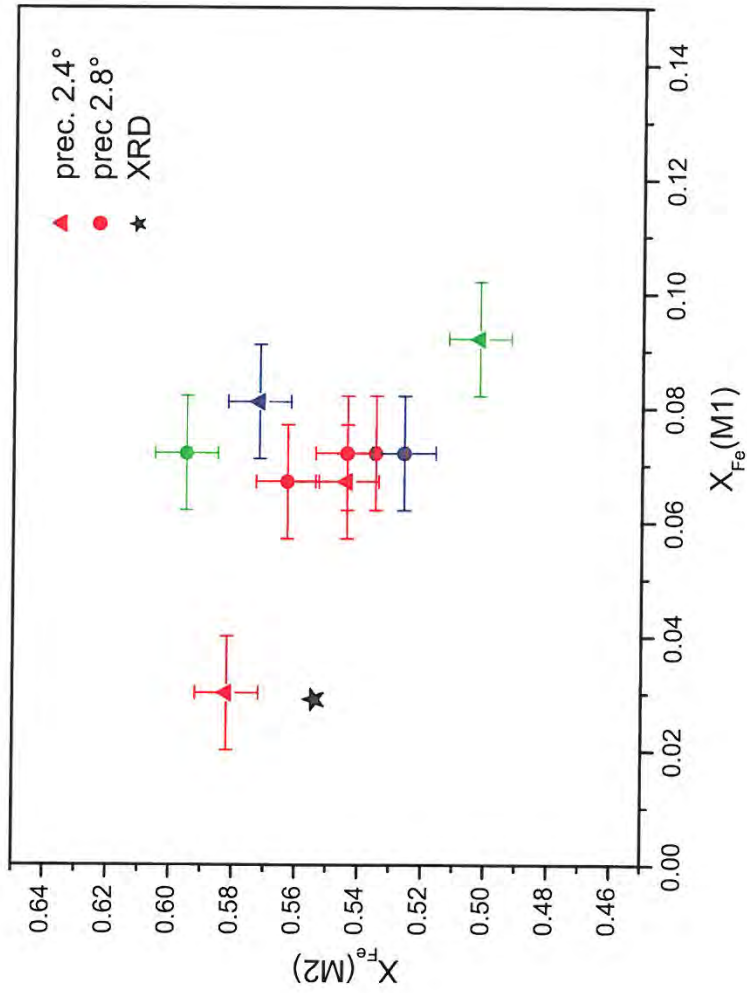


Figure 5

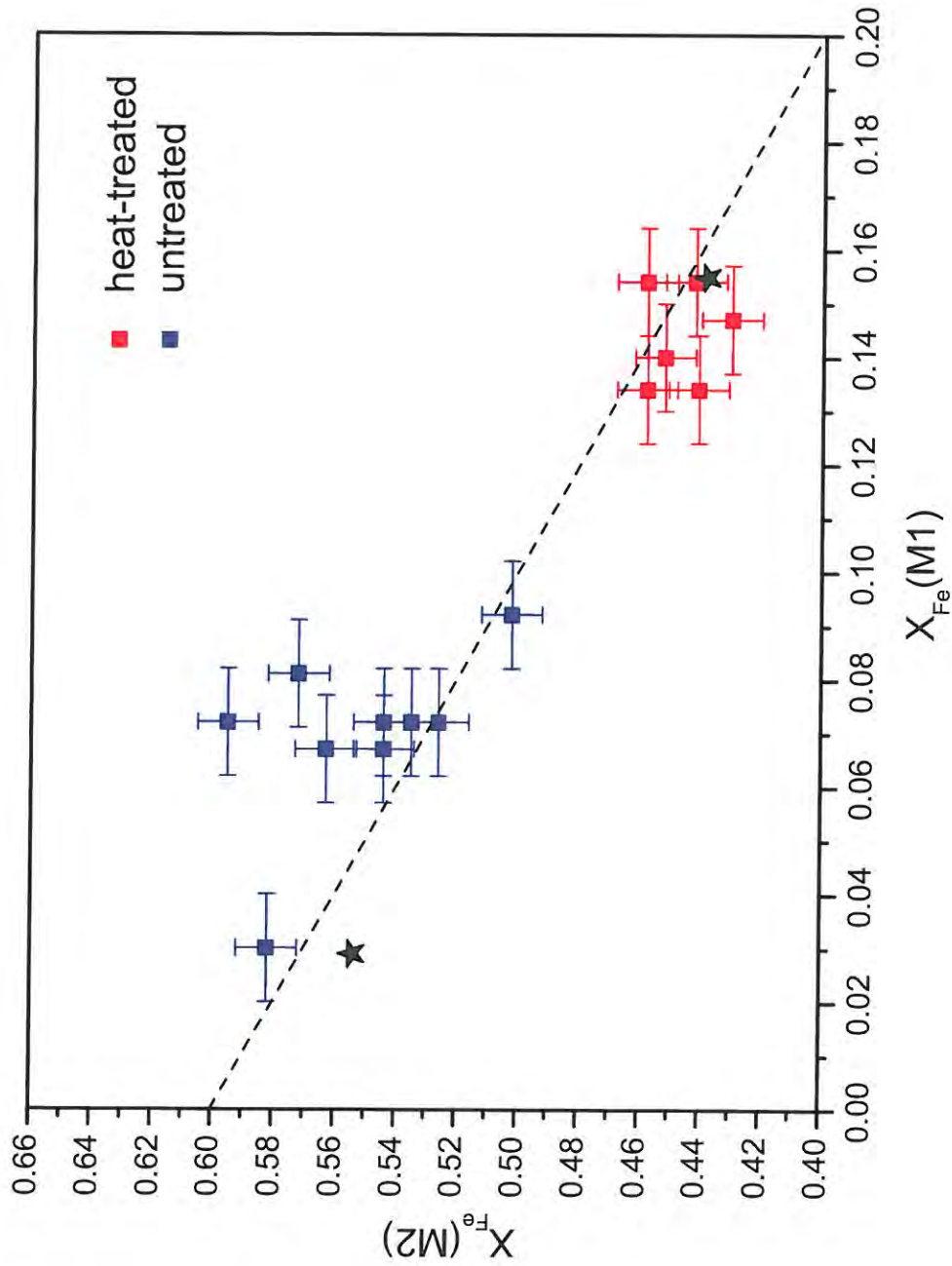


Figure 6

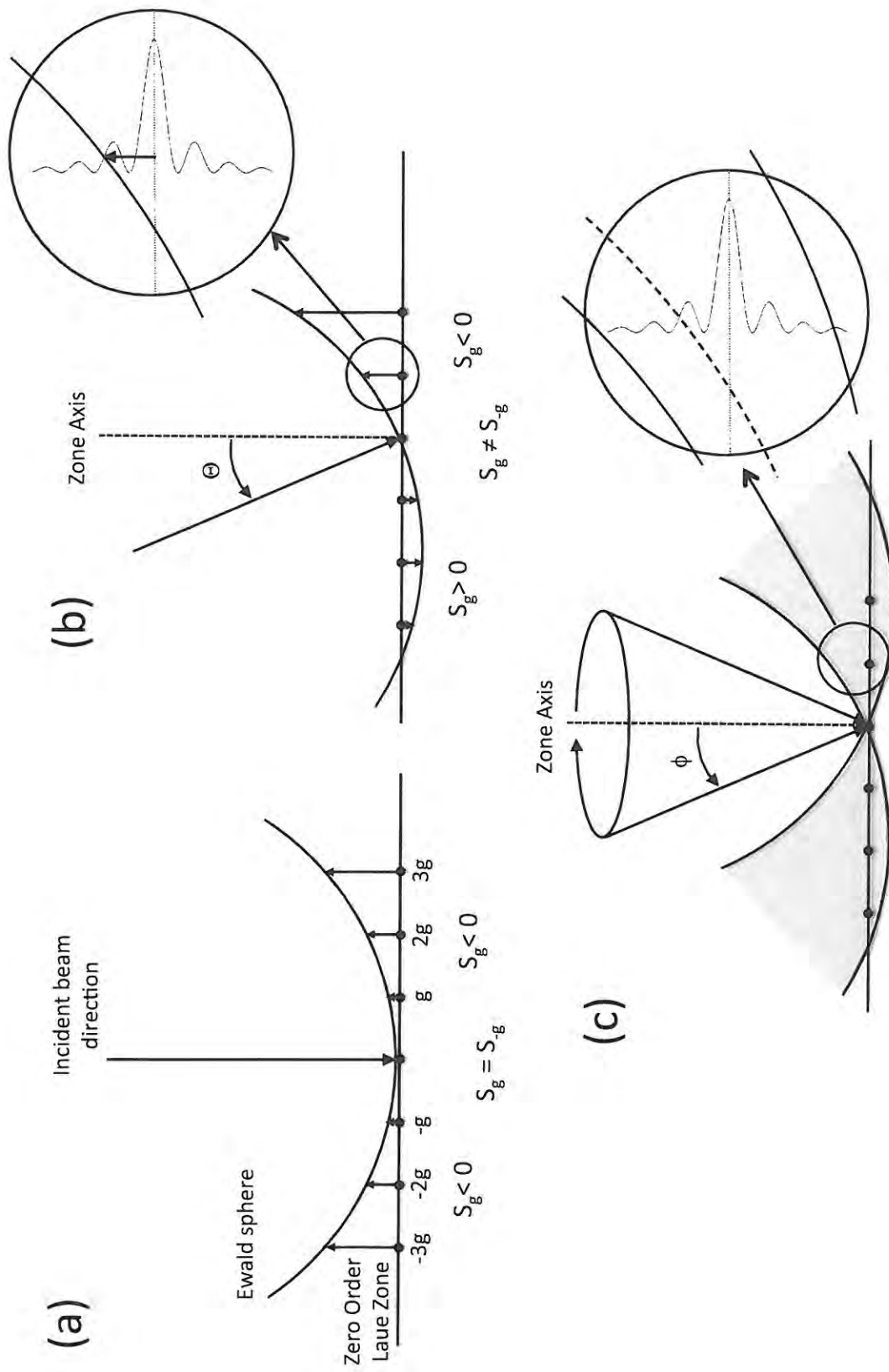


Figure 7